RESEARCH ARTICLE

ADVANCED
INTELLIGENT
SYSTEMS
Open Access

www.advintellsyst.com

Regulating Airflow Using Hybrid LCN for Soft Pneumatic Circuits

Elif Kurt, Youssef M. Golestani, Efstathios Barmpoutsis, Sergio Picella, Robin L. B. Selinger, Johannes T. B. Overvelde,* and Danqing Liu*

Being flexible and adaptive to various environments, soft robotics shows promise as a more robust alternative in many applications compared to traditional, rigid robotics. Of many employable different actuation strategies, pneumatically driven soft robotics have gained attraction owing to their relative straightforward manufacturing and capability to produce significant force to their environment upon interaction. To enable more autonomous pneumatic systems, however, there is an emerging need for developing smarter fluidic elements responding to environmental cues, to provide embodied control and regulation. Herein, a liquid crystal network (LCN)-based fluid regulator is designed to impart stimuli responsiveness and regulation into fluidic circuits by combining radially aligned nematic and nonaligned isotropic LCNs. Assisted by a finite element method, the thermoresponsiveness of the LCN is discussed. Finally, the regulating behavior of the responsive pneumatic regulator is demonstrated, which alters its fluidic resistance with changing temperature. This work emphasizes the potential of advancing responsive soft robotics that can interact with their environment through multiphysical stimuli.

1. Introduction

Soft robotics is reshaping the future of robotics by transforming rigidity into flexible and adaptive bodies which can exhibit embodied intelligence for sophisticated and safe human–machine interactions.[1–4] With integration of soft technologies and soft systems, new advanced machines can be developed to improve the communication between user and machine or between machines mutually for various applications. This opens up many fields such as wearable soft robotics,[5,6] bioinspired systems,[7,8] biomedical applications,[9,10] gripping, sorting, and manipulating of objects.[11,12]

Pneumatically actuated soft robotics continues to be one of the main technologies in the soft robotics field owing to its affordability, applicability, fast response time, and capability of producing adaptive and complex motions resulting from large and nonlinear deformations.[13–15] Even though ample pneumatic actuators have been developed, it remains challenging to develop hardware that is compliantly soft to power and control the actions of the soft robot. In many cases, soft pneumatic robots still rely on pumps and compressors as the power source to provide the driving force for the pneumatic actuation.[16,17] Moreover, the internal fluid pressure in each actuator is typically regulated by solenoid valves that need an electrical energy input to activate and that cannot be easily embedded in the robot.[1,17] Research has been done to integrate soft fluidic elements for pressure control and regulation within fluidic circuits that substitute electronic control, yet the structures that have been used for regulatory and control systems predominantly consist of passive materials, limiting the possibility of changing behavior in response to external cues.[18,19]

E. Kurt, Y. M. Golestani, D. Liu
Department of Chemical Engineering and Chemistry
Human Interactive Materials (HIM)
Eindhoven University of Technology
Groene Loper 3, 5612 AE Eindhoven, Netherlands
E-mail: danqing.liu@tue.nl

E. Kurt, Y. M. Golestani, S. Picella, J. T. B. Overvelde, D. Liu
Institute for Complex Molecular Systems (ICMS)
Eindhoven University of Technology
5600 MB Eindhoven, Netherlands
E-mail: overvelde@amolf.nl

The ORCID identification number(s) for the author(s) of this article can be found under https://doi.org/10.1002/aisy.202401069.

E. Barmpoutsis
Polymer Technology Group/Eindhoven (PTG/e) B.V.
De Lismortel 31, 5612 AR Eindhoven, Netherlands

S. Picella, J. T. B. Overvelde
Autonomous Matter Department
AMOLF
Science Park 104, 1098 XG Amsterdam, Netherlands

R. L. B. Selinger
Department of Physics
Kent State University
Kent OH 44242, USA

J. T. B. Overvelde
Department of Mechanical Engineering
Eindhoven University of Technology
P.O. Box 513, 5600 MB Eindhoven, Netherlands

**ADVANCED
SCIENCE NEWS**

www.advancedsciencenews.com

**ADVANCED
INTELLIGENT
SYSTEMS**

www.advintellsyst.com

To achieve smarter soft robotic devices, we need to design and develop regulatory systems that impart responsiveness. Eventually, integrating responsive behavior into devices can introduce embedded regulation and control systems, which are essential to avoid bulky equipment and complex tubing to move forward in autonomous soft robotics.[1,8,20]

To achieve this purpose, incorporating active responsive materials into fluidic circuits provides an interesting multiphysics approach. Here, we focus on incorporating liquid crystal (LC) materials to enable responsive and regulating behaviors, which originate from their capability of producing anisotropic mechanical response at the microscale. We demonstrate that such liquid crystal networks (LCNs) enable stimuli-responsive fluid regulators. We integrate these regulators into pneumatic systems and showcase the usage of heat to control their open-and-close behavior which we also describe by computational simulations. Consequently, we achieved embedded regulation with the developed smart LCN fluid regulator in response to thermal stimuli by altering the fluidic resistance of the LCN.

2. Results and Discussion

2.1. Configuration of the Nematic-Isotropic Hybrid LCN Film

We designed our LCN fluid regulator with slits created in the center and confined in an aluminum holder for integration in fluidic systems, where its actuation can be triggered by controlled thermal stimuli under airflow, as shown in **Figure 1**A. For the LCN fluid regulator, we introduced active (aligned nematic) and passive (nonaligned isotropic) layers to form a hybrid bilayer structure. The underlying principle of the actuation is based on the LCN anisotropic properties: the aligned nematic layer will contract along the molecular director with increasing temperature, whereas the isotropic layer will expand in all directions (Figure 1B). This thermal response results in the bending behavior of the LCN segments, forming a positive curvature toward the nematic side.

We prepared our LC monomer mixtures by dissolving the compounds in dichloromethane. Chemical structures of these compounds are given in Figure 1C. Monomer **1** is the LC diacrylate, and monomers **2** and **3** are the LC monoacrylates, respectively. We added UV-absorber **4** to induce light intensity gradient over the thickness of the polymer film. We carried out photopolymerization in the presence of photoinitiator **5** which has an optical absorption that overlaps with **4**. We added a small amount of thermal inhibitor **6** to our LC monomer mixture to avoid premature polymerization. We fabricated our hybrid LCN regulator by following a two-step polymerization procedure within glass cells, as illustrated in Figure 1D. Initially, we established planar molecular alignment across the LC film. We induced photopolymerization-induced diffusion driven by the light-intensity gradient along the film thickness caused by the UV absorber (molecule **4**).[21–23] Prior to the polymerization steps, we performed experiments to investigate the absorbance of LC mixture with varying molecule **4** concentration and sample thickness. We kept the cell thickness constant for the experiments with varying molecule **4** concentration and observed that as the concentration increased, the absorbance also increased. We observed that
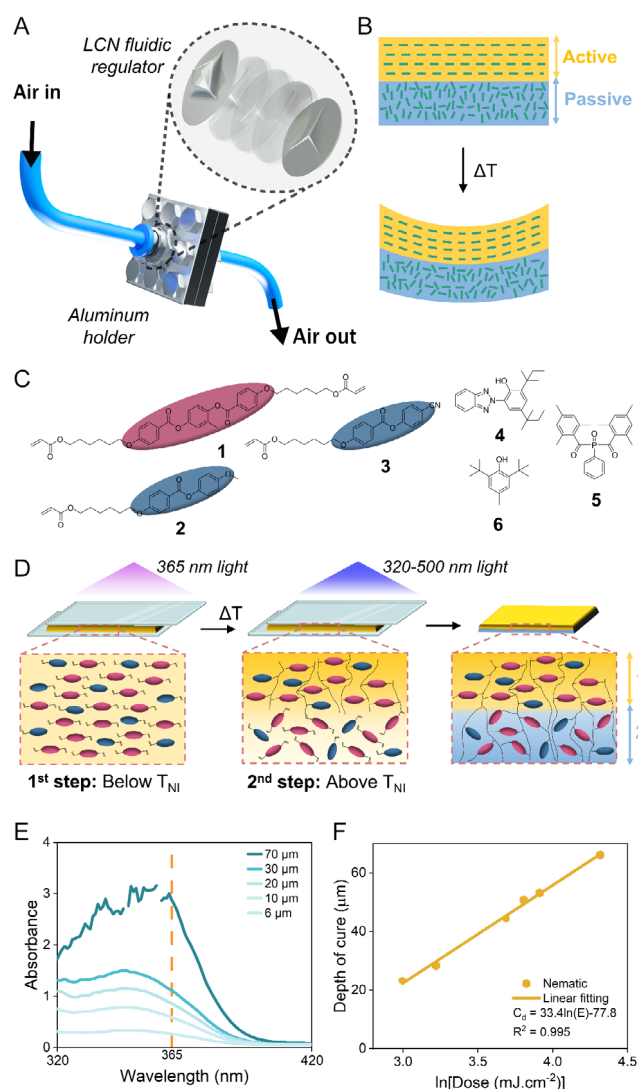

Figure 1. Principle of the hybrid LCN regulator. A) Schematic representation of the LCN fluid regulator and thermal actuation of the LCN segments under controlled airflow. B) Illustration of the bending motion of the unidirectionally aligned hybrid LCN with increasing temperature. Molecular alignments are shown with green dashes within the aligned nematic (active) layer and nonaligned isotropic (passive) layer, indicated as gold and blue, respectively. C) Chemical structures of the compound that were used for the fabrication of LCNs. D) The two-step polymerization procedure. Orientation and crosslinking of LC molecules for each step were shown as inset drawings. Gold region 1 represents the active, whereas blue region 2 represents the passive layer. E) UV/VIS spectra of LC mixture having 1 wt% of molecule **4** with respect to thickness of LC mixture. F) Cure depth of nematic layer (C_d) against irradiation dose (E) at 365 nm.

high concentrations of molecule **4** resulted in disturbed LC alignment which might be causing changes in the Frank elastic constants that are not energetically favorable.[24] Consequently, molecule **4** will aggregate, forming clusters that result in nonuniform local heating across the film.[25–27] For the rest of the experiments, we chose to use 1 wt% of molecule **4**. Additionally, we observed an increasing absorbance of LC films with increasing sample thickness, as shown in Figure 1E. To withstand pressures

compatible with soft robotic applications, we opted for a 70 μm thickness of the LC film to have enough bending stiffness of the film against airflow while allowing sufficient bending.

Next, we determined the optimum energy dose for photopolymerization. Because of the existence of molecule 4 in the mixture, LC monomers were crosslinked to form the aligned active layer on the light-irradiated side of the film in the first step of polymerization, as seen in Figure 1D. The thickness of the polymerized nematic layer was controlled by the exposed energy dose, showing a relationship in agreement with the literature (Figure 1F).[28] Subsequently, we polymerized the remaining LC mixture in the lower region of the glass cell at isotropic state at elevated temperature above T_{NI} ($T_{NI} \approx 67\,°C$, see Figure S1, Supporting Information for dynamic scanning calorimetry (DSC) analysis before polymerization steps). Eventually, we achieved covalently bonded aligned active layer and nonaligned passive layer, as shown in Figure 1D.

We further confirmed the formation of the hybrid nematic/isotropic LCNs by using scanning electron microscopy (SEM). We varied energy doses for the polymerization of the nematic layer. As shown in **Figure 2**A, the cross-sectional SEM images indicate two distinct covalently bonded layers with a contrast in brightness. We assume that the brightness difference originates from the density and structural differences between the nematic and isotropic layers. The isotropic LCN is loosely packed, leading to lower density compared to that of the nematic LCN.[29] This can lead to secondary electrons (SE) penetrating deeper into the low-density isotropic LCN and lose more energy before leaving the surface to be collected by the detector, which results in darker images.[30] Additional to SE, we imaged the cross section with backscattered electrons (BSE), as shown in Figure 2B. The high-density nematic LCN layer was darker under SEM with BSE (Figure 2B(ii)). As BSE can penetrate deeper into the materials compared to SE, the darker nematic layer can be attributed to the reduced signal intensity caused by the energy loss within denser networks.[30,31] Note that no contrast was distinguished when the LCN film is only composed of isotropic layer, which was established as the reference to support our hypothesis (Figure 2B(iii), see also Figure S2, Supporting Information). Moreover, we observed that the thicknesses of the high-density nematic LCN
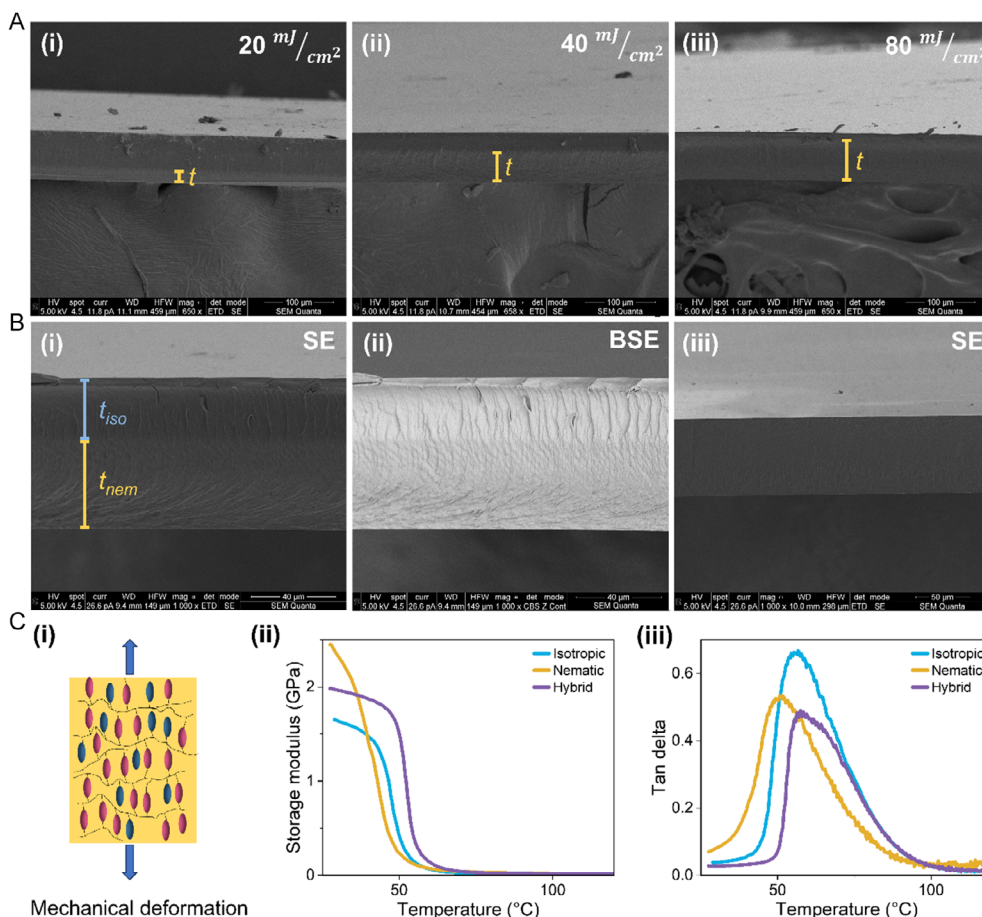

Figure 2. Characterization of the hybrid LCN film. A) SEM images of cross section of the LCN bilayers. Active layers (bottom) were polymerized with energy doses of (i) 20 mJ cm⁻², (ii) 40 mJ cm⁻², and (iii) 80 mJ cm⁻². The thickness of the active layers for each image was indicated as t. B) SEM images of the (i) LCN bilayer polymerized with an energy dose of 40 mJ cm⁻² with secondary electrons, (ii) LCN bilayer polymerized with an energy dose of 40 mJ cm⁻² with BSEs, and (iii) isotropic LCN with secondary electrons. Layer thicknesses for nematic, t_{nem}, and isotropic, t_{iso}, were indicated with gold and blue bars, respectively. C) DMTA results of the 70 μm-thick bilayer, nematic and isotropic LCN strips. (i) Illustration of the mechanical deformation direction, (ii) storage modulus of the LCN strips, and (iii) tan delta of the LCN strips.

layers were consistent with energy dose measurements in Figure 1F.

We aimed to optimize the mechanical properties of the LCN by creating a hybrid bilayer. First, we performed dynamic mechanical thermal analysis (DMTA) on a hybrid LCN for the analysis of mechanical properties. We prepared the specimen for the analysis such that molecular alignment was parallel to the mechanical deformation direction (Figure 2C(i)). We observed that the bilayer has an integrated storage modulus of 2 GPa at room temperature, as shown in Figure 2C(ii), which is common for glassy LCNs.[32,33] As control experiments, we studied samples with uniform nematic alignment and isotropic alignment, individually. At room temperature, we observed the highest storage modulus for the nematic LCN strip, due to its high order throughout the thickness compared to the isotropic LCN and the hybrid LCN.[29] These results also confirmed that the contrast in SEM images was caused by differences in mechanical properties, leading to different fracturing of the layers (Figure 2B). The analysis revealed that the glass transition temperature (T_g) was around 55 °C for all the samples, obtained from tan delta peaks (Figure 2C(iii)). Nevertheless, we observed a postponed decrease in the mechanical properties to relatively higher temperatures ($\approx$10 °C for storage modulus of the hybrid LCN), following the small differences in T_g of the samples, as can be seen in Figure 2C(ii,iii). We note here that the storage modulus of all samples dropped to nearly 20 MPa at temperatures above T_g.

2.2. Thermal Actuation of the LCN Regulator

We utilized the newly developed hybrid LCN by using it as a temperature-responsive pneumatic regulator. To allow for future integration into fluidic circuits and soft robots, we aimed to achieve open-and-close actuation from the center of the bilayer. To observe the thermal responsiveness of the LCN regulator, we assembled an aluminum holder to confine a hybrid LCN at its peripheral boundary (**Figure 3**A). We performed two-step polymerization as described in Figure 1D to obtain radially aligned hybrid LCN films within the glass cells in which the alignment layer was controlled by photopatterning. Inspired by previous studies, we created the triwing-shaped slits in the center to achieve open-and-close actuation (Figure 3B, see the *Experimental Section* for more information).[34,35] Another important prerequisite is to align the center of the slit in the sample with the core of the defect. Because of the peripheral confinement, the lateral actuation was restricted to actuate only from the center and avoid saddle-shape formation caused by the radial alignment of the molecules.[36] Due to the actuation mechanism explained in Figure 1B in combination with such confinement, the LCN segments can create positive curvature toward the nematic side with increasing temperature. We schematically demonstrate this in the inset of Figure 3A.

To confirm the effect of the cut and peripheral boundary condition, we performed finite element method (FEM) modeling where we incorporate the gradient in the crosslink density caused by the UV irradiation during the photopolymerization (see Figure S3, Supporting Information). The simulation results revealed that having slits is essential to form positive curvature

toward nematic side, which was not observed for the models without the slits in their geometry. Additionally, having a peripheral confinement that restricts the deformations only to the center of the samples was justified by our simulations (see Figure S4, Supporting Information).

We investigated the thermal responsiveness of the LCN regulator in a controlled environment, without applying any airflow yet. Initially, the LCN segments were mostly flat with a minor out-of-plane deformation toward the isotropic side, most likely due to the formation of the slits at the temperature above room temperature. Upon increasing temperature, the LCN segments started to actuate, generating a positive curvature toward the nematic side due to the contraction of the nematic layer in the alignment direction and the expansion of the isotropic layer (Figure 3C). The maximum deformation was detected at 105 °C, which defines the open state. The reverse behavior was observed upon cooling. At 50 °C, the system reached its closed state, where the open area of the regulator was minimal. Further cooling below 50 °C caused an out-of-plane deformation toward the isotropic side. The simulation results during thermal actuation are shown in Figure 3D(i) with a red arrow indicating the decrease in nematic order of the mesogenic units (see Supporting Information for more information). Magnified tetrahedral mesh of the center of the LCN segments in open state is shown in Figure 3D(ii). The simulated deformation is shown with normalized color plot in Figure 3D(iii), where the largest displacement appeared at the tips of the slits. To prevent out-of-plane deformation toward the isotropic side, we designed a solid support at the bottom part of the aluminum holder to be in contact with isotropic layer as shown in Figure 3E. Utilizing the new design, the out-of-plane deformation was eliminated even below the room temperature, as shown in Figure 3F.

Next, we examined the actuation of the LCN segments for two consecutive heating cycles. We analyzed the displacement of the tip of the nematic side of the hybrid LCN segment (Figure 3G). The segments only started to bend from the center of the sample, showing a drastic increase at 60 °C which is around T_g. The two cycles exhibited similar trends. However, we observed stagnation followed by a sharp increase in the second cycle, indicating a sudden snapping instability. This can be explained by the fact that the segments obstructed each other prior to snapping taking place. The normalized displacements obtained from simulation upon thermal actuation were also shown with red triangles in Figure 3G for temperatures above T_g. For simplicity, we plotted the normalized displacements as a function of κ, a dimensionless order parameter scaled with the mechanical properties (see Supporting Information for more information). While our model fitted well with the experimental data, we note here that we did not observe linear behavior as expected, which was reported previously for a setup with similar model.[37] We believe that this might be due to the polymerization-induced diffusion and creation of the slits within the sample.

Before integrating our hybrid LCN into fluidic circuits, we investigated the effect of the thickness of active nematic layer, as well as the geometry of the slits using FEM simulations. We found out that the deformation of the LCN segments increases as the thickness of the active layer increases and saturates after 50 μm, validating our choice of energy dose during the first step of photopolymerization (see Figure 1D,F). We note that
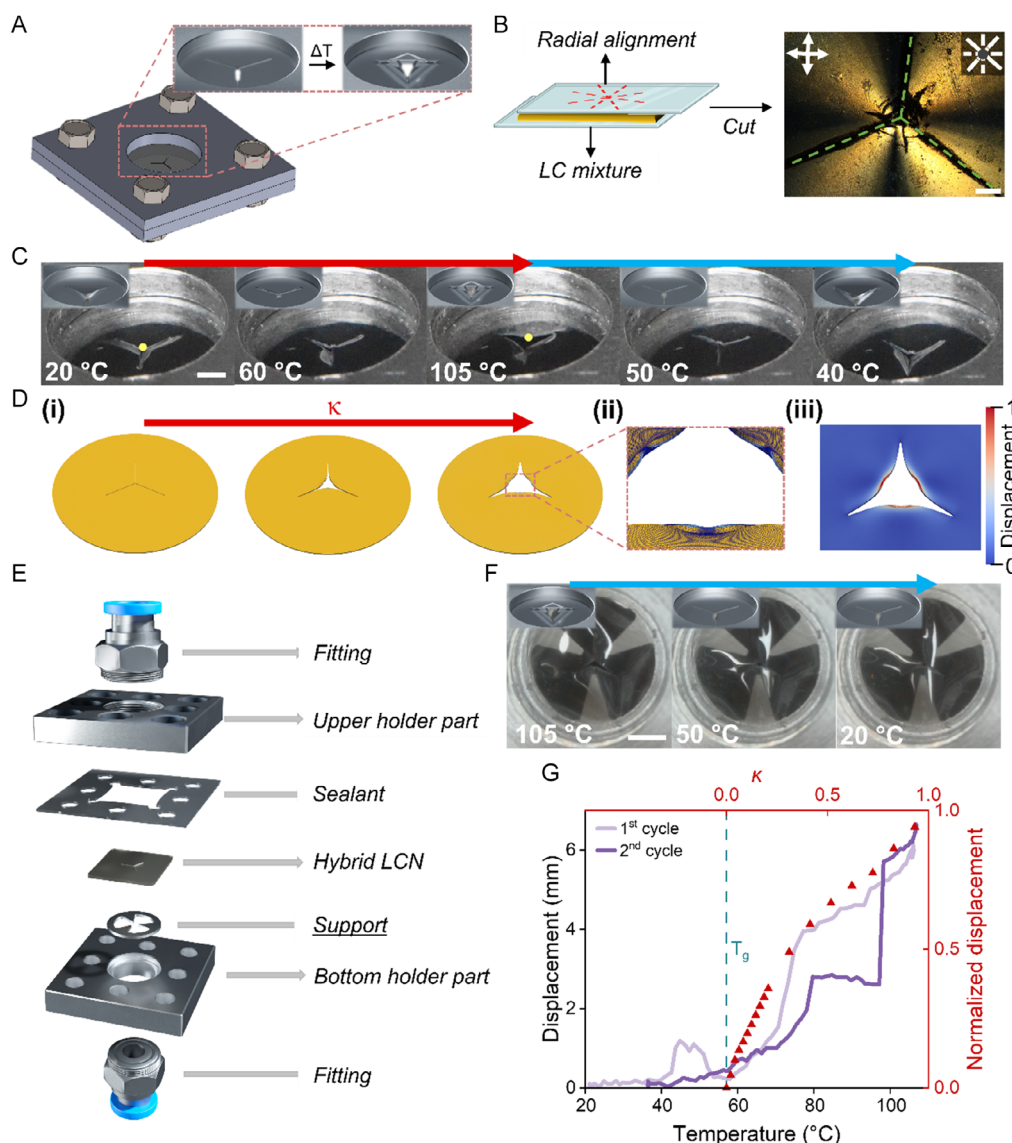
Figure 3. Thermal actuation of the hybrid LCN segments. A) Representative drawing of the aluminum holder for confining the hybrid LCN for thermal actuation. The inset shows the actuation of the LCN segments in response to temperature. B) Schematic representation of the cell and POM image of the hybrid LCN with radial alignment. The green dashes highlight the slits. Scale bar: 250 µm. C) Photographs of the confined hybrid LCN actuated thermally; heated up from 20 °C to 105 °C, indicated with a red arrow, and cooled down from 105 to 40 °C, indicated with a blue arrow. 3D drawings of the LCN segments were given as inset. Scale bar: 2 mm. D) FEM simulation of the confined hybrid LCN upon reducing scaler order parameter: (i) initial closed state, $\kappa = 0$ (left), at $\kappa = -0.518$ (middle), and final open state, $\kappa = -1.033$ (right). Nematic and isotropic layers are indicated with gold and blue, respectively. (ii) Magnified center area of the slits in open state including the triangular mesh. (iii) Color plot of the normalized displacement in open state. E) Annotated 3D illustration of aluminum holder for confining the hybrid LCN with solid support. F) Photographs of the confined hybrid LCN with solid support for cooling down from 105 to 20 °C. 3D drawings of the LCN segments were given as inset. Scale bar: 3 mm. G) Displacement of the tip of the upper nematic segment for 2 consecutive heating cycles. The data were obtained from yellow dots in (C). The normalized displacement from the simulation is shown with red triangles.

while the thickness of active layer influenced the displacement, it also affected the shape of the hybrid LCN (see Figure S5, Supporting Information). Furthermore, we examined different geometries for the slits by varying the length of the cut (*L*) within the hybrid LCN with respect to the radius (*R*) of the sample. As shown in Figure S6, Supporting Information, our modeling results revealed that the deformations increase as *L*/*R* increases and saturates after 0.4, which was the ratio used in our experiments.

2.3. Controlling Airflow in the Fluidic Circuit with the Integration of the LCN Fluid Regulator

We further integrated our hybrid LCN into a fluidic regulation system to observe the actuation under controlled airflow with varying temperatures. For the experiments, the cell was kept in an environment with a controlled constant temperature. A wall-mounted pressure regulator and a flow controller were
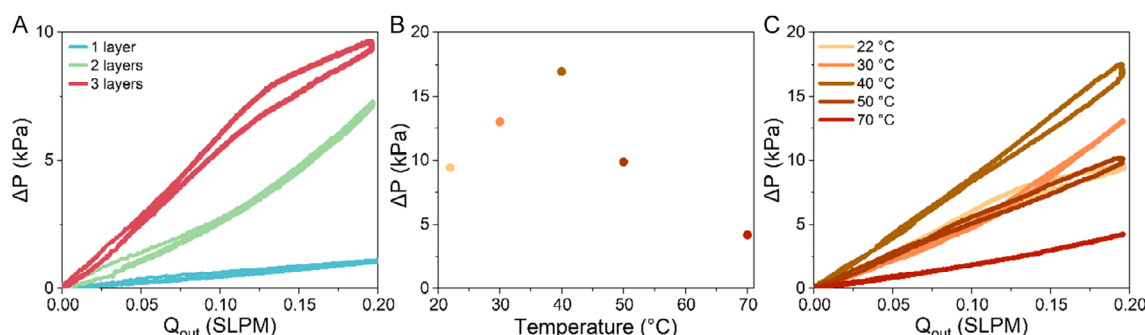
2401069 (5 of 9)

**ADVANCED
SCIENCE NEWS**

www.advancedsciencenews.com

**ADVANCED
INTELLIGENT
SYSTEMS**
Open Access

www.advintellsyst.com

Figure 4. Responsive LCN regulator integrated into fluidic system. A) Pressure drop versus outlet airflow rate with regulator consisting of various stacks at room temperature. Slope of the curves gives the fluidic resistance at corresponding stacking of the LCNs. B) Pressure drop measured across three stacked LCN regulators with respect to temperature at $Q \approx 0.2$ SLPM. C) Fluidic resistance with three stacked LCN regulators at corresponding temperatures.

introduced in the flow circuit, as can be seen in Figure S7, Supporting Information. A pressure sensor was used to monitor the pressure drop across the hybrid LCN. To enhance the structural robustness against high pressures, we utilized multilayered stacking of the LCNs by stacking them in close contact. This is due to the fact that fluidic resistance, R_{flow}, increased with increasing the number of the hybrid LCN layers which can be inferred from the slope of the curves ($R_{flow} = \Delta P/Q_{out}$) in **Figure** 4A, where ΔP and Q_{out} are the pressure drop across the stacked LCN regulators and outlet flow rate, respectively (see also Figure S8, Supporting Information).[38] Initially, there was a minor out-of-plane deformation toward isotropic side caused by the fabrication as described earlier in the *Thermal Actuation of the LCN Regulator* section, which caused an increase in pressure drop until the regulator closes at 40 °C. As expected, by further increasing temperature, the regulator started to open and, subsequently, the pressure drop decreased as shown in Figure 4B. There is always an airflow present through the slits, yet, we observed that fluidic resistance altered as the regulator is thermally activated, as can be deduced from the slope of curves given in Figure 4C. We obtained the highest fluidic resistance when the regulator is in its closed state. The results demonstrated that the developed hybrid LCN film can be utilized as fluidic resistance regulator in fluidic circuits, owing to its regulating behavior in response to changing temperature.

3. Conclusion

In this work, we designed an LCN system to introduce responsive fluid regulator for integrating fluidic circuits for the first time. We obtain radially aligned hybrid LCN films consisting of active and passive layers via polymerization-induced diffusion to impart thermal responsiveness and modify mechanical properties of the LCN. Assisted by a computational approach, we design and fabricate responsive LCN with variable flow resistance regulated by temperature. We successfully incorporate this newly developed thermoresponsive LCN regulator within fluidic circuits to demonstrate its regulating behavior by altering the fluidic resistance of the hybrid LCN. We envision that by introducing airflow with varying temperatures to control

thermal responsiveness within the fluidic circuit, embedded self-regulation can be achieved.

The proposed responsive fluid regulators demonstrate significant potential, yet, it remains open to further advancements, refinements, and explorations. Although the reversible thermal actuation was observed for one layer of LCN regulator without introducing airflow, the stacked LCN fluid regulators failed to demonstrate the same behavior upon cooling under controlled airflow. We foresee that this can be resolved by developing thicker LCN regulators that can stand for high pressures rather than using close contact stacking of thin film LCN regulators, or designing regulators in different geometries. Additionally, conducting quantitative studies to understand the effects of temperature and the flow rate of the imposed air could provide valuable insights, since the actuation of the LCN segments might be affected by the interplay between the different heat transfer modes; however, this was beyond the scope of the present study. Herein, we have presented insights into the use of active LC materials that can be incorporated into pneumatic soft robotic systems to regulate fluid flow at a proof-of-concept level. Our work highlights the potential toward the development of constructing multiphysics fluidic soft robots by combining active and passive materials into hybrid structures for tunable mechanical properties and introducing stimuli-responsive properties for embedded intelligence. With this approach, we anticipate advancements to move forward in the development of more intelligent and autonomous soft fluidic robotics by demonstrating the inclusion and innovation of hybrid materials with different geometries.

4. Experimental Section

Materials: The reactive mesogens 1,4-Bis[4-(6-acryloyloxyhexyloxy)benzoyloxy]-2-methylbenzene (molecule **1**) and 4-methoxyphenyl 4-(6-Acryloyloxyhexyloxy)benzoate (molecule **2**) were purchased commercially from Daken Chemical Limited and 4-Cyanophenyl 4-((6-(acryloyloxy)hexyl)oxy)benzoate (molecule **3**) was purchased commercially from Merck UK. UV-absorber Tinuvin 328 (molecule **4**) was obtained from BASF. Photoinitiator Bis(2,4,6-trimethylbenzoyl)-phenylphosphineoxide (molecule **5**) was received from CIBA. Inhibitor butylated hydroxytoluene (molecule **6**), dichloromethane (DCM), and N,N-dimethylformamide (DMF) were received from Sigma–Aldrich. Polyimide Optmer AL 1254 Display

Material was purchased from JSR Micro. Photoalignment agent (SD1) was received from Nanjing JingCui Optical Technology Co., LTD, Nanjing, China. All chemicals and solvents were used without further purification.

Fabrication of Glass Cells: Glass substrates were cleaned with acetone and isopropanol in an ultrasonicator for 20 min, respectively. After drying them under nitrogen stream, they were placed in a UV-ozone chamber for 20 min. For obtaining planar alignment of LC mesogens, Optmer AL 1254 was spin coated on the glass substrates at first 800 rpm for 5 s, then 5000 rpm for 40 s. After spin coating, the glass substrates were prebaked on a hot plate at 100 °C for 10 min and cured in an oven at 180 °C for 3 h. To induce unidirectional planar alignment, the coated-glass substrates were rubbed with a velvet cloth in one direction, then glued to each other antiparallelly by using a UV glue containing the glass beads as spacers to separate the glass substrates with a desired thickness (the diameter of the glass beads used were 6 µm, 10 µm, 20 µm, 30 µm, and 70 µm). To obtain radial alignment of LC mesogens, 0.3 wt% SD1 in DMF was spin coated on clean glass substrates at first 800 rpm for 8 s, then 3000 rpm for 40 s. After spin coating, the glass substrates were annealed for 5 min on a hot plate at 108 °C to remove DMF completely. Glass substrates were glued to each other by using a UV glue containing 70 µm spacers to fabricate cells. Then, the fabricated glass cells were patterned by using digital micromirror device (DMD)-based dynamic microlithography to obtain radial alignment in the cell.

Preparation of Liquid Crystal Network Mixtures and Films: Monomer mixtures were prepared by mixing molecules **1**, **2**, and **3** in the ratio of 32.5 wt%, 48.8 wt%, and 16.3 wt%, respectively. 1 wt% of molecule **4**, 1 wt% of molecule **5**, and 0.5 wt% of molecule **6** were added to the mixture, subsequently. To obtain a homogeneous mixture, all the materials were dissolved in DCM (1 mL), which was evaporated afterward. For UV-Vis spectrophotometry, monomer mixtures were prepared with changing fractions of molecule **4** ranging in between 0.1 and 2.0 wt%, without adding molecule **5** to avoid photopolymerization during measurements. The glass cells were filled with the LCN mixture at 80 °C (above $T_{NI} \approx 67$ °C before polymerization steps) by capillary action. The filled glass cells were cooled down to 50 °C with a rate of 5 °C min^{-1} under nitrogen atmosphere and waited 10 min prior to photopolymerization for LC molecules to align within the cells and stabilize the alignment. Then, by using 365 nm light with a collimator (Thorlabs M365L2-C2 and Thorlabs SM2F32-A, respectively), the samples were illuminated from the top with low intensities (4 mW cm^{-2}) for different exposure times to satisfy the desired energy doses to polymerize the nematic layer to form the active part of the LCN bilayer. After that, the temperature was increased to 100 °C to obtain isotropic LCN mixture on the bottom of the glass cell to form the passive layer after polymerization. After waiting for 5 min at 100 °C, the samples were photopolymerized by using Exfo Omnicure S2000 light source with high intensity (25 mW cm^{-2}). Then, the samples were postcured on a hot plate at 120 °C for 10 min and allowed to slowly cool down to room temperature. After postbaking, the glass cells were opened with razor blade and the covalently bonded hybrid LCNs were removed which were obtained from the same LC mixture polymerized at its nematic phase for active layer and isotropic phase for passive layer. Subsequent to polymerization and removal of the radially aligned hybrid LCNs from the glass cell, the triwing-shaped slits were created by using a custom-made triwing-shaped cutter after adjusting the center of the slits with the core of the defect.

Depth of Cure Measurements: Only the first step of polymerization was carried out for the depth of cure measurements. 70 µm-thick planar glass cells were fabricated and filled with the LC mixture having 1.0 wt% of molecule **4**. The samples were polymerized at 50 °C with 1 mW cm^{-2} intensity with 365 nm light with different exposure times to vary the energy dose that was exposed. Then, the cells were opened and the thin films were rinsed thoroughly with acetone to get rid of the unreacted part of the mixture. The samples were dried totally in a vacuum oven at 40 °C overnight prior to the thickness measurements with optical profilometry.

Material Characterization: The analysis for phase transition of LC monomer mixture was performed with DSC on a Discovery 2500 from TA Instruments. For DSC measurements, monomer mixture was prepared without a photoinitiator to prevent polymerization during measurements.

Within 3 consecutive cycles, the sample was heated to 150 °C and cooled down to −50 °C with a rate of 5 °C min^{-1} for both heating and cooling. The absorption spectra of LC monomer mixtures were obtained within 300–800 nm wavelengths by using UV/VIS/NIR Spectrometer Perkin Elmer Lambda750 to examine the absorbance of the molecule **4** with respect to molecule **4** concentration and sample thickness. Signals were smoothened via Origin with embedded-in adjacent-averaging method with 3 points of window. For in situ photopolymerizations of the LCN mixtures within glass cells at different polymerization temperatures and intensities, observing the transition temperature and checking the alignment after polymerization, Leica CTR6000 polarized optical microscope equipped with Leica DFC420C camera was used. Linkam temperature control stage was used to control the temperature during observations. 3D optical profilometry measurement was done by using Sensofar S Neox from ST Instruments for depth of cure analysis. To determine the mechanical properties of thin LCN films, dynamic mechanical thermal analysis (DMTA) was conducted by using Q800 DMA from TA Instruments, operated in multifrequency-strain mode from room temperature to 150 °C with a rate of 5 °C min^{-1}, with applying a preload force of 0.0100 mN. The oscillation amplitude and frequency were set to 15.0 µm and 1 Hz, respectively. The LCN bilayer was formed with an energy dose of 40 mJ cm^{-2} for DMTA. To observe the actuation with temperature, the one bilayer was confined in between two aluminum plates which has a circular shaped window in the center and the assembly was placed in an oven. The sample was heated from 20 to 105 °C inside the oven with a rate of 5 °C min^{-1}. The heater of the oven was switched off to let the samples slowly cool down inside the oven. The temperature inside the oven was recorded by using SHT35-DIS-B temperature and humidity sensor. Images of the actuation of the hybrid LCN bilayer were recorded with Olympus digital camera with 15 s and 90 s of time intervals for heating and cooling cycles, respectively. The displacement calculations were done by image analysis where the tip of one LCN bilayer segment was tracked with a custom script without any modifications on the frames. For SEM imaging, the LCN strips were sputter-coated with 12 nm gold layer by using Quorum Q 150T S plus SEM coating system for 30 s with 30 mA. The cross section of the LCN strips was observed by operating FEI SEM Quanta 3D FEG at 5 kV in both secondary electron mode and BSE mode.

Actuation within Flow Circuit: Fluidic circuit consisted of wall-mounted pressure regulator (LRP-1/4/10, Festo), 0.75 L air tank (CRVZS-0,75, Festo), mass flow controller (SLA5800, Brooks Instrument), ±34.5 kPa pressure sensor (SSCDRRN005PDAA5, Honeywell), and mass airflow sensor (AWM5101VN, Honeywell) to regulate and characterize the pressures and flows in the fluidic circuit (Figure S7, Supporting Information). The radially aligned LCN hybrid regulators were confined within a custom-made aluminum holder for integration in fluidic circuits with a solid support which was used at the isotropic LCN side to avoid out-of-plane deformation toward isotropic side of the LCN segments (see Figure 3E). The LCNs were placed in the aluminum holder to ensure a 60° angle between the triwing-shaped cuts and the arms of the solid support. The temperature of the aluminum holder was controlled by a heating oven, with an average heating rate of 3 °C min^{-1} (UF30, Memmert). For controlling experiment and data acquisition, a USB-powered I/O device (NI USB-6212, National Instruments) and a custom software were used. A custom MATLAB script was used to interpret the data. The fluidic circuit was tested for air tightness with and without the fluid regulator before starting the measurements. All measurements were carried out with a data acquisition frequency of 1000 Hz with 15 s of blank measurement for sensor offset. A total of 4 actuation cycles were performed at each temperature for various stacks of the LCN layers. When stacked, the LCN layers were set 30° offset from each other. Only the aluminum holder was kept in the heating oven for thermal actuation of the LCN bilayers. Fluidic cycles were started 10 min after the desired temperature was reached to stabilize the temperature of the aluminum holder and allow the hybrid LCN to actuate in response to temperature. For each fluidic cycle, the flow rate was increased from 0 to 0.2 SLPM (standard liter per minute) in 20 s, held at 0.2 SLPM for 15 s, and decreased to 0 SLPM in 20 s. The last 3 cycles were taken into account out of 4 cycles when analyzing the data for each

2401069 (7 of 9)

measurement, and the average of the 3 cycles is given for the corresponding temperature and stacking as the analysis results.

Finite Element Modeling: Actuation of the bilayer LCN was obtained using a finite element method elastodynamics with tetrahedral mesh, adapted to the model described in ref. [39]. See Supporting Information for more information.

Supporting Information

Supporting Information is available from the Wiley Online Library or from the author.

Conflict of Interest

The authors declare no conflict of interest.

Author Contributions

Elif Kurt: data curation (lead); formal analysis (lead); investigation (lead); methodology (lead); project administration (supporting); validation (lead); visualization (lead); writing—original draft (lead); writing—review editing (equal). **Youssef M. Golestani**: data curation (lead); formal analysis (lead); investigation (lead); methodology (lead); validation (lead); visualization (supporting); writing—original draft (lead); writing—review editing (equal). **Efstathios Barmpoutsis**: formal analysis (supporting); methodology (supporting); writing—review editing (supporting). **Sergio Picella**: formal analysis (supporting); methodology (supporting); writing—review editing (supporting). **Robin L. B. Selinger**: formal analysis (supporting); methodology (supporting); resources (supporting); writing—review editing (supporting). **Johannes T. B. Overvelde**: conceptualization (equal); funding acquisition (equal); methodology (equal); project administration (equal); resources (equal); supervision (equal); writing—review editing (equal). **Danqing Liu**: conceptualization (lead); funding acquisition (lead); methodology (lead); project administration (lead); resources (lead); supervision (lead); writing—review editing (lead).

Data Availability Statement

The data that support the findings of this study are available from the corresponding author upon reasonable request.

Keywords

fluid regulators, liquid crystal polymer networks, polymerization-induced diffusion, responsive materials, soft robotics

[1] C. D. Onal, *Micro- and Nanotechnology Sensors, Systems, And Applications VIII*, SPIE, Bellingham, WA **2016**, p. 983627.

[2] J. Walker, T. Zidek, C. Harbel, S. Yoon, F. S. Strickland, S. Kumar, M. Shin, *Actuators* **2020**, *9*, 3.

[3] C. D. Onal, D. Rus, *Bioinspiration Biomimetics* **2013**, *8*, 026003.

[4] D. Rus, M. T. Tolley, *Nature* **2015**, *521*, 467.

[5] G. Agarwal, N. Besuchet, B. Audergon, J. Paik, *Sci. Rep.* **2016**, *6*, 34224.

[6] M. Zhu, S. Biswas, S. I. Dinulescu, N. Kastor, E. W. Hawkes, Y. Visell, in *Proc. of the IEEE*, Institute of Electrical and Electronics Engineers Inc., Piscataway, NJ **2022** *110*, 246.

[7] S. Kim, C. Laschi, B. Trimmer, *Trends Biotechnol.* **2013**, *31*, 287.

[8] S. I. Rich, R. J. Wood, C. Majidi, *Nat. Electron.* **2018**, *1*, 102.

[9] M. Cianchetti, C. Laschi, A. Menciassi, P. Dario, *Nat. Rev. Mater.* **2018**, *3*, 143.

[10] P. Polygerinos, Z. Wang, K. C. Galloway, R. J. Wood, C. J. Walsh, *Rob. Autom. Syst* **2015**, *73*, 135.

[11] S. Zou, S. Picella, J. de Vries, V. G. Kortman, A. Sakes, J. T. B. Overvelde, *Nat. Commun.* **2024**, *15*, 539.

[12] J. Shintake, V. Cacucciolo, D. Floreano, H. Shea, *Adv. Mater.* **2018**, *30*, 1707035.

[13] N. Vasios, A. J. Gross, S. Soifer, J. T. B. Overvelde, K. Bertoldi, *Soft Rob.* **2020**, *7*, 1.

[14] M. S. Xavier, C. D. Tawk, A. Zolfagharian, J. Pinskier, D. Howard, T. Young, J. Lai, S. M. Harrison, Y. K. Yong, M. Bodaghi, A. J. Fleming, *IEEE Access* **2022**, *10*, 59442.

[15] D. Onal Cagdas, X. Chen, G. M. Whitesides, D. Rus, *Robotics Research* (Eds: H. I. Christensen, O. Khatib), Springer, Cham **2017**.

[16] S. Xu, C. M. Nunez, M. Souri, R. J. Wood, *Sci. Rob.* **2023**, *8*, eadd4649.

[17] M. S. Xavier, A. J. Fleming, Y. K. Yong, *IEEE Rob. Autom. Lett.* **2021**, *6*, 5800.

[18] L. C. van Laake, J. de Vries, S. Malek Kani, J. T. B. Overvelde, *Matter* **2022**, *5*, 2898.

[19] L. C. Van Laake, A. Comoretto, J. T. B. Overvelde, *J. Fluids Struct.* **2024**, *126*, 104090.

[20] G. M. Whitesides, *Angew. Chem. Int. Ed.* **2018**, *57*, 4258.

[21] D. J. Broer, G. N. Mol, J. A. M. M. Van Haaren, J. Lub, *Adv. Mater.* **1999**, *11*, 573.

[22] D. J. Broer, J. Lub, G. N. Mol, *Nature* **1995**, *378*, 467.

[23] Y. Zhan, G. Zhou, B. A. G. Lamers, F. L. L. Visschers, M. M. R. M. Hendrix, D. J. Broer, D. Liu, *Matter* **2020**, *3*, 782.

[24] C. L. Van Oosten, K. D. Harris, C. W. M. Bastiaansen, D. J. Broer, *Eur. Phys. J. E* **2007**, *23*, 329.

[25] A. H. Gelebart, G. Vantomme, E. W. Meijer, D. J. Broer, *Adv. Mater.* **2017**, *29*, 1606712.

[26] G. Vantomme, A. H. Gelebart, D. J. Broer, E. W. Meijer, *J Polym. Sci. A Polym. Chem.* **2018**, *56*, 1331.

[27] J. P. F. Lagerwall, G. Scalia, *Curr. Appl. Phys.* **2012**, *12*, 1387.

[28] S. C. Ligon, R. Liska, J. Stampfl, M. Gurr, R. Mülhaupt, *Chem. Rev.* **2017**, *117*, 10212.

[29] D. J. Broer, R. A. M. Hikmet, G. Challa, *Die Makromol. Chem.* **1989**, *190*, 3201.

[30] W. Zhou, R. P. Apkarian, Z. Lin Wang, D. Joy, *Scanning Microscopy For Nanotechnology* (Eds: W. Zhou, Z. L. Wang), Springer, New York, NY **2006**.

[31] G. E. Lloyd, *Mineral. Mag.* **1987**, *51*, 3.

[32] R. A. M. Hikmet, D. J. Broer, *Polymer* **1991**, *32*, 1627.

[33] D. Liu, D. J. Broer, *Langmuir* **2014**, *30*, 13499.

[34] H. Zeng, O. M. Wani, P. Wasylczyk, R. Kaczmarek, A. Priimagi, *Adv. Mater.* **2017**, *29*, 1701814.

[35] C. D. Modes, M. Warner, C. Sánchez-Somolinos, L. T. De Haan, D. Broer, in *Proc. of the Royal Society A: Mathematical, Physical and Engineering Sciences*, Royal Society, England **2013**, *469*, 20120631.

[36] L. T. De Haan, A. P. H. J. Schenning, D. J. Broer, *Polymer* **2014**, *55*, 5885.

[37] Y. You, Y. M. Golestani, D. J. Broer, T. Yang, G. Zhou, R. L. B. Selinger, D. Yuan, D. Liu, *Mater. Horiz.* **2024**, *11*, 3178.

[38] A. Sengupta, *Int. J. Mol Sci.* **2013**, *14*, 22826.

[39] A. H. Gelebart, D. Jan Mulder, M. Varga, A. Konya, G. Vantomme, E. W. Meijer, R. L. B. Selinger, D. J. Broer, *Nature* **2017**, *546*, 632.